Supplementary Material

Analysis of the structure of nanocomposites of triglyceride platelets and DNA

Martin Schmiele[1], Charlotte Knittel[1], Sebastian Busch,[2] Humphrey Morhenn,[1,3] Peter Boesecke,[4] Sérgio S. Funari[5], Ralf Schweins,[6] Peter Lindner,[6] Martin Westermann,[7] Frank Steiniger,[7] and Tobias Unruh[1]

[1] *Professur für Nanomaterialcharakterisierung (Streumethoden), Friedrich–Alexander–Universität Erlangen–Nürnberg, Staudtstr. 3, 91058 Erlangen, Germany*

[2] *German Engineering Materials Science Centre (GEMS) at Heinz Maier-Leibnitz Zentrum (MLZ), Helmholtz-Zentrum Geesthacht GmbH, Lichtenbergstr. 1, 85748 Garching, Germany*

[3] *Forschungs-Neutronenquelle Heinz Maier-Leibnitz (FRM II), Lichtenbergstr. 1, 85747 Garching, Germany*

[4] *European Synchrotron Radiation Facility (ESRF), 71 Avenue des Martyrs, CS40220, 38042 Grenoble CEDEX 9, France*

[5] *HASYLAB at DESY, Notkestr. 85, 22607 Hamburg, Germany*

[6] *DS / LSS, Institut Laue-Langevin (ILL), 71 Avenue des Martyrs, CS20156, 38042 Grenoble CEDEX 9, France*

[7] *Center for Electron Microscopy of the Jena University Hospital, Ziegelmühlenweg 1, 07743 Jena, Germany*

A Electron densities and neutron scattering length densities of the stabilizer molecules and DNA

For the electron densities (EDs) ρ^{X} and neutron scattering length densities (NSLDs) ρ^{n} of the shells physically meaningful range specifications were imposed in the fits: Lecithin molecules possess a distinct contrast between their phosphocholine head groups (without additional water molecules: $\rho^{\mathrm{X}} = 514\,\mathrm{nm}^{-3}$, $\rho^{\mathrm{n}} = 1.88 \cdot 10^{-6}\,\mathrm{Å}^{-2}$ [1]) and their acyl chains (depending on the degree of unsaturation and length, typically $\rho^{\mathrm{X}} = 270 \ldots 280\,\mathrm{nm}^{-3}$, $\rho^{\mathrm{n}} = -0.1 \cdot 10^{-6} \ldots -0.4 \cdot 10^{-6}\,\mathrm{Å}^{-2}$ [1, 2]). For a DODAB molecule (Fig. 1(e)), similar values for the EDs and NSLDs for the acyl chains (18:0) and head group are found. The contrast between the hydrophilic PEG ($\rho^{\mathrm{X}} = 350\,\mathrm{nm}^{-3}$, $\rho^{\mathrm{n}} = 0.60 \cdot 10^{-6}\,\mathrm{Å}^{-2}$) and hydrophobic PPG blocks ($\rho^{\mathrm{X}} = 332\,\mathrm{nm}^{-3}$, $\rho^{\mathrm{n}} = 0.34 \cdot 10^{-6}\,\mathrm{Å}^{-2}$) in PLX (Fig. 1(c)) is much lower. For TW (Fig. 1(d)), with its monooleate (18:1) chain and a head group consisting of 20 PEG blocks partitioned onto 4 branches, the EDs and NSLDs are nearly the same as for the lecithin chains and pure PEG blocks. The ED for DNA (without further water molecules) is about $540\,\mathrm{nm}^{-3}$ and thus on the order of the lecithin head groups. The NSLD is about $4 \cdot 10^{-6}\,\mathrm{Å}^{-2}$ in D_2O. D_2O at 25 °C has $\rho^{\mathrm{X}} = 333\,\mathrm{nm}^{-3}$ and $\rho^{\mathrm{n}} = 6.3 \cdot 10^{-6}\,\mathrm{Å}^{-2}$.
Usually the inner shell is dedicated for the lipophilic parts of the stabilizer molecules (in this study: fatty acid residues for S100, DODAB and TW; PPG blocks for PLX) and the outer shell for their hydrophilic parts (phosphocholine head groups for S100, dimethylammonium head group for DODAB and essentially PEG blocks for TW and PLX) and the DNA.
However, such a separation is quite difficult in the present study because of the different structures of the molecules. While S100, DODAB and TW share a certain similarity in their acyl chain and head group (on average TW's head groups are only 5 PEG units long) lengths, the situation for S100, DODAB and PLX is different. PLX is expected to adopt a U-conformation with the PPG blocks being flatly condensed at the nanocrystal surfaces. But the two hydrophilic 80-PEG-units-long branches are structurally very different to the rather small head groups of DODAB and S100 and might protrude much farther into the dispersion medium. Furthermore for the complexes, it cannot be ruled out that the sandwiched DNA partially penetrates into the inner shell.
Thus the concept to separate the stabilizer's lipophilic parts into the inner shell and its hydrophilic parts (plus the DNA) into the outer shell may oversimplify the problem. A reliable differentiation between the individual stabilizer molecules and the DNA in such complicated mixtures is challenging (e.g. similar ED and NLSD for chains of DODAB and S100; similar EDs for the lecithin head group and DNA).
Thus, in the fits, the range of EDs and NSLDs in both shells was set to the minimum and maximum values of the EDs and NSLDs of the involved molecules and dispersion medium: $270 \ldots 540\,\mathrm{nm}^{-3}$ for the EDs and $-0.5 \cdot 10^{-6} \ldots 6.3 \cdot 10^{-6}\,\mathrm{Å}^{-2}$ for the NSLDs.

B Trimyristin suspensions

B.1 Native trimyristin suspensions

Native trimyristin (MMM, Dynasan®114, 98%, Sasol GmbH, Witten, Germany) suspensions were prepared to screen for stable suspensions whose colloidal platelets can form sandwich-like assemblies with DNA. The aqueous suspensions were prepared from MMM (10%) and stabilized by the lecithin blend S100 (2.4%) and different types and amounts of cationic stabilizers. We use the abbreviation ⟨y⟩-x, where ⟨y⟩ denotes the different cationic stabilizers: Dimethyldioctadecylammonium bromide (DODAB, 98%, Fig. S1(a), Sigma-Aldrich Chemie GmbH, Taufkirchen, Germany), Dioleoyltrimethylammonium propane (DOTAP, Fig. S1(b), Lipoid AG, Ludwigshafen, Germany), Cetylpyridinium chloride (CPYC, 99%, Fig. S1(c), Sigma-Aldrich Chemie GmbH, Taufkirchen, Germany), and those of the alkyltrimethylammonium bromide series: C_6TAB (98%, Fig. S1(g)), C_{10}TAB (99.9%, Fig. S1(f)), C_{12}TAB (98%, Fig. S1(e)) (all from TCI Deutschland GmbH, Eschborn, Germany) and C_{16}TAB (98%, Fig. S1(d), Merck, Darmstadt, Germany). x denotes the concentration of the cationic stabilizer (0.4 or 1.2%). For example, CPYC-0.4 denotes a MMM suspension, co-stabilized with 0.4% CPYC.

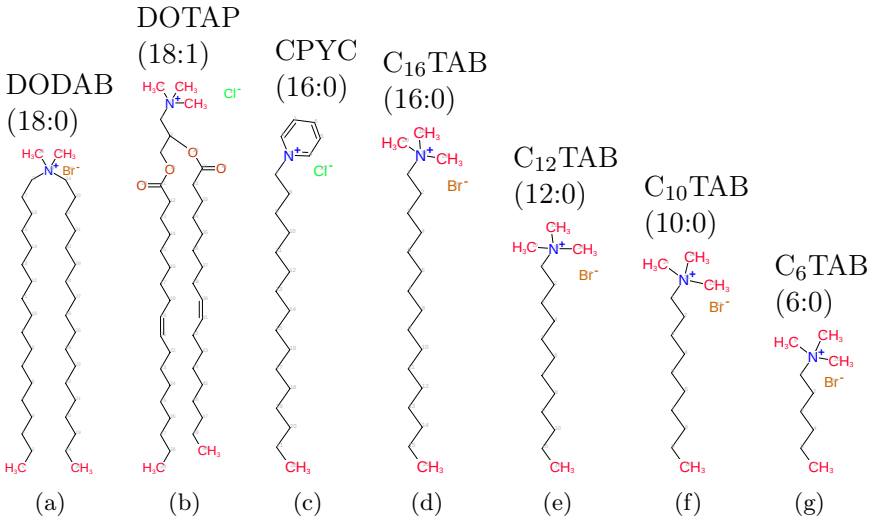

Figure S1: Molecular structures of the stabilizers used in the study of the MMM suspensions.

All cationic stabilizers are quaternary ammonium compounds. They differ in their head group and the number, length and degree of unsaturation of their hydrophilic carbon chains. The single-tailed C_6TAB, C_{10}TAB, C_{12}TAB, C_{16}TAB of the alkyltrimethylammonium bromide series share the same head group and differ only in their chain lengths. CPYC has the same chain length as C_{16}TAB, but has a pyridinium head group. The double-tailed surfactant DOTAP shares the same chain length with DODAB, but has mono-unsaturated chains.

B.1.1 Preparation of the native MMM suspensions

MMM and S100 were heated to 65 °C until a clear yellowish melt was obtained. H_2O was heated to the same temperature. While the surfactants DODAB and DOTAP were mixed with the melt, CPYC and the cationic surfactants of the alkyltrimethylammonium bromide series were dissolved in H_2O. The hot mixture was pre-dispersed for 3 minutes with an Ultra-Turrax T25 Basic disperser (IKA-Werke GmbH & Co. KG, Staufen, Germany) at 22.000 rpm.
1 ml of the hot MMM pre-emulsion was filled into a reaction tube. An MS 73 ultrasonic needle of a Sonopuls ultrasonic homogenizer (Bandelin electronic, Berlin, Germany) was immersed to a maximum depth of 2 cm in the pre-emulsion, avoiding any contact with the surrounding reaction tube, and the pre-emulsion was sonicated for 5 min in a pulsed mode.
Formulations with 0.4% cationic stabilizers (CPYC, C_{10}TAB, C_{12}TAB, C_{16}TAB), which upon ultrasonication and crystallization provided stable suspensions with PCS measured z-averages for the hydrodynamic diameters below 250 nm, were further considered. The formulations with C_6TAB, DODAB and DOTAP solidified.

Table SI: z-averaged hydrodynamic particle diameters (d_{PCS}) and polydispersity indices (PdI) for native MMM suspensions. Furthermore, the enthalpies of fusion (ΔH_{fus}) and crystallization (ΔH_{cry}), derived from the μDSC heating and cooling runs in Fig. S2(a), are listed. $\Delta H^*_{\mathrm{fus}}$ denotes the enthalpy of fusion associated with the melting of particles with an unknown triglyceride modification.

	PCS		μDSC			
sample	d_{PCS} [nm]	PdI [-]	ΔH_{fus} [J/g]	$\Delta H^*_{\mathrm{fus}}$ [J/g]	$\frac{\Delta H^*_{\mathrm{fus}}}{\Delta H_{\mathrm{fus}}}$ [%]	ΔH_{cry} [J/g]
CPYC-0.4	126.5	0.18	15.9	1.8	11.3	-15.4
CPYC-1.2	149.8	0.18	16.1	4.6	28.6	-15.8
C_{16}TAB-0.4	126.6	0.14	16.5	1.4	8.5	-15.5
C_{16}TAB-1.2	158.1	0.21	15.6	3.2	20.5	-15.0
C_{12}TAB-0.4	117.1	0.18	14.4	0.8	5.4	-14.1
C_{12}TAB-1.2	142.8	0.15	16.4	1.0	6.4	-14.4

To obtain smaller particle sizes, the hot MMM pre-emulsions of three successful candidates (CPYC, C_{12}TAB, C_{16}TAB with 0.4% and 1.2% cationic stabilizer) were passed to an APV-2000 high-pressure melt homogenizer (APV Deutschland GmbH, Unna, Germany) which was preheated to a temperature of about 70 °C. About 40 ml of the samples were homogenized in a closed loop for four minutes with gradually increasing pressures between 1 and 1.5 kbar. The MMM nanoemulsions were allowed to cool down to room temperature and finally stored in crimped glass vials at 6 °C. In contrast to tripalmitin nanoemulsions, which crystallize above room temperature, cooling below 10 °C is crucial to crystallize MMM nanoemulsions, because of a strong super-cooling effect for triglyceride nanoemulsions [3].
The crystallization of triglyceride emulsion droplets into the thin platelets of the stable β-modification is accompanied by a vigorous surface expansion. To cover quickly the newly created surfaces of the platelets, it is assumed that highly mobile co-stabilizers are required, to prevent a gelation [4]. The double-tailed surfactants DODAB and DOTAP are too slow to stabilize the nanoparticles upon crystallization. The single-tailed cationic surfactants can diffuse faster. The reason why C_6TAB cannot stabilize the dispersion successfully is not yet understood.

B.1.2 PCS measurements

The z-averaged hydrodynamic diameters d_{PCS} and the corresponding polydispersity indices of the selected native MMM suspensions are listed in Tab. SI. All suspensions possess polydisperse particle size distributions. The d_{PCS}-values, which can be regarded as a rough estimate of the platelet diameters, vary between about 120 and 150 nm. The size distributions show moderate polydispersity indices between 0.14 and 0.21.

B.1.3 µDSC measurements

The DSC heating and cooling curves of the MMM dispersions are visualized in Fig. S2(a). Between about 26 °C and 56 °C (melting point of bulk MMM) many partially overlapping melting peaks can be observed in the heating curve. For temperatures between 35 and 56 °C these peaks can be attributed to the melting of platelets in the β-modification (dashed box labelled by β), where each peak corresponds to the melting of platelets with a specific thickness [5]. In particular for the CPYC and C_{16}TAB stabilized suspensions between 29 and 34 °C another broad melting peak can be observed. Increasing the concentration of CPYC and C_{16}TAB from 0.4% to 1.2%, the fraction of the enthalpy of fusion of this pre-transition $\Delta H^*_{\mathrm{fus}}$ (integrated in the range 26 - 35 °C, dashed box with the question mark) with respect to the total enthalpy of fusion ΔH_{fus} (integrated over the full heating run) rises by a factor of more than 2 (Table SI). For the C_{12}TAB stabilized suspensions this pre-transition is much weaker and does not change with C_{12}TAB concentration.
Such pre-transitions can be attributed to a melting of cLNP adopting the thermodynamically metastable α-modification of MMM (bulk m.p. 33 °C [6]) or to a fraction of smaller platelets with an unknown MMM modification, as it was reported for tyloxapol stabilized MMM suspensions with a pre-transition between 30 °C and 38 °C [7].

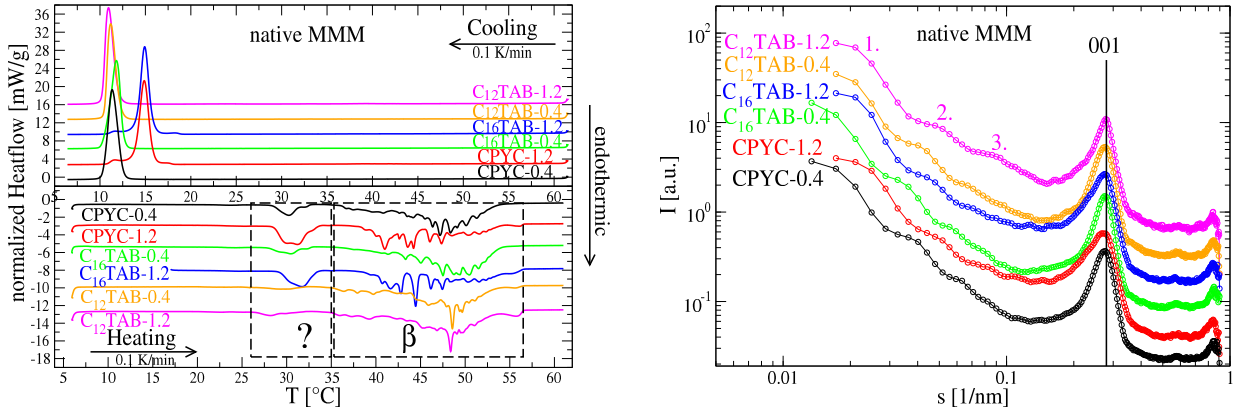

(a) (b)

Figure S2: (a) µDSC heating and cooling scans recorded between 5 °C and 60 °C and (b) SAXS patterns (Hecus camera) of the native MMM suspensions. For clarity, in (a) the curves were shifted vertically in steps of 3.5 mW/g (cooling) and −2.5 mW/g (heating), starting from the curve of CPYC-0.4. Boxes framed with dashed lines in the plot of the heating curves mark the temperature ranges associated with the melting of platelets in the unknown (?) and β-MMM modification. In (b) the SAXS pattern are shifted by factors of 2 starting from the bottom. The position of the 001 Bragg reflection of bulk β-MMM is marked by a vertical line. For C_{12}TAB-1.2 the first three stack-related peaks are marked with numbers.

The subsequent cooling curves in Fig. S2(a) exhibit a strong super-cooling of the molten cLNP. Except for C_{16}TAB-1.2 and CPYC-1.2, the cooling curves exhibit a single crystallization event starting at 13.3 °C, with peak positions between 11 °C and 12 °C. The main crystallization peaks are shifted to slightly higher temperatures for C_{16}TAB-1.2 (15.0 °C) and CPYC-1.2 (14.8 °C). Furthermore, their peak is preceded and followed (again at about 11.5 °C) by small shoulders. The higher crystallization temperatures for C_{16}TAB-1.2 and CPYC-1.2 can be explained by the increased chain length and higher concentration of their cationic stabilizers. Stabilizers with longer saturated alkyl chains can increase the crystallization temperature of emulsion droplets, as it was shown for lecithin stabilized triglyceride dispersions [8].

B.1.4 SAXS measurements

The SAXS patterns of the MMM suspensions and their cLNP-DNA complexes were measured with a Kratky camera (S3-MICROpix, Hecus X-Ray Systems GmbH, Graz, Austria) at FRM II in Garching, Germany. The 50 W Cu K_α ($\lambda = 1.54$ Å) microfocus X-ray source (Xenocs, Sassenage, France) was equipped with a 3D single bounce mirror optics, focusing the primary beam into the detector plane. The collimator was adjusted to deliver a beam of about $0.25 \times 0.25\,\mathrm{mm}^2$ at the sample position, leading to a total flux of about 10^7 photons/s. The samples and water were measured in a reusable quartz capillary with an inner diameter of about 1 mm. Exposures were taken at 25 °C for one hour with a Pilatus 100K detector (Dectris AG, Baden, Switzerland). The sample-detector distance of 289.5 mm was calibrated with a silver behenate standard (Eastman Kodak Company). A secondary standard (glassy carbon [9]) was used to put the scattered intensities on an absolute scale.

The SAXS patterns of the native MMM suspensions are visualized in Fig. S2(b). At $s = 0.280\,\mathrm{nm}^{-1}$ the SAXS patterns feature the 001 Bragg reflection of MMM nanocrystals in the β-modification [10]. Since the platelets possess a thickness of only a few molecular layers of MMM, the 001 Bragg peak is strongly broadened. In particular for CPYC-1.2 and C_{16}TAB-1.2 the Bragg peak becomes asymmetric. This could be associated with a Bragg reflection, stemming from the unknown MMM modification.

For all suspensions, the diffuse small-angle scattering intensity is super-imposed by at least three peaks, indicating a lamellar order in the dispersion (for C_{12}TAB-1.2 labelled by 1, 2 and 3 in Fig. S2(b)). These additional reflections can be attributed to a self-assembly of the triglyceride platelets into stacks [11, 12]. The platelet repeat distances in these stacks range between 40 and 50 nm for the different suspensions.

B.2 MMM-DNA complexes

cLNP-DNA complexes were prepared from the MMM suspensions CPYC-x, C_{16}TAB-x, C_{12}TAB-x with charge ratios ξ between ∞ (no DNA) and 0.3 and final MMM concentrations of 1% or 3% MMM. cLNP-DNA complexes with low charge ratios (0.3, 0.5, 0.7 and 1) often solidified or larger agglomerates became visible. For the same charge ratios, cLNP-DNA complexes prepared from native suspensions with 1.2% of the cationic stabilizer tend to agglomerate more easily compared to those with only 0.4%, probably because the total amount of added DNA is three times higher in the former dispersions.

B.2.1 PCS measurements

Table SII: (a) z-averaged hydrodynamic diameters (d_{PCS}) and polydispersity indices (PdI) for cLNP-DNA complexes (3% MMM) prepared from CPYC-0.4. Starred fields (*) indicate measurements with $d_{\mathrm{PCS}} > 1\,\mu$m. (b) Total enthalpies of fusion (ΔH_{fus}) and crystallization (ΔH_{cry}) for cLNP-DNA complexes (3% MMM) prepared from CPYC-1.2. ΔH_{fus} and ΔH_{cry} are obtained from the μDSC heating and cooling curves in Fig. S3(a). $\Delta H^{\dagger}_{\mathrm{fus}}$ and $\Delta H^{\dagger}_{\mathrm{cry}}$ denote the enthalpy of fusion and crystallization associated with the melting of large platelet agglomerates observed in the dashed boxes in Fig. S3(a).

(a)

PCS		
ξ [-]	d_{PCS} [nm]	PdI [-]
0.3	*	*
0.5	*	*
0.7	*	*
1	*	*
2	*	*
3	908.8	0.22
10	129.3	0.20
∞	127.3	0.17

(b)

μDSC						
ξ [-]	ΔH_{fus} [J/g]	$\Delta H^{\dagger}_{\mathrm{fus}}$ [J/g]	$\frac{\Delta H^{\dagger}_{\mathrm{fus}}}{\Delta H_{\mathrm{fus}}}$ [%]	ΔH_{cry} [J/g]	$\Delta H^{\dagger}_{\mathrm{cry}}$ [J/g]	$\frac{\Delta H^{\dagger}_{\mathrm{cry}}}{\Delta H_{\mathrm{cry}}}$ [%]
0.3	4.4	4.4	100.0	-3.70	-3.70	100.0
1	5.4	1.8	33.9	-4.70	-1.27	27.0
2	5.3	0.8	15.2	-5.03	-0.67	13.3
5	5.4	0.7	13.2	-5.04	-0.52	10.2
∞	5.0	0.2	4.6	-4.62	-0.00	0.0

d_{PCS} values in the sub-micron range were found only for small amounts of added DNA ($\xi \geq 3$). By way of example, for cLNP-DNA complexes (3% MMM) prepared with CPYC-0.4, the d_{PCS}-values and the polydispersity indices are listed in Table SII(a).

B.2.2 µDSC measurements

The increased agglomeration of the platelets with decreasing charge ratio manifests also in the microcalorimetric heating and cooling runs. As an example, for cLNP-DNA complexes prepared from CPYC-1.2 (3% MMM), the heating and cooling runs are visualized in Fig. S3(a).

Upon addition of DNA, a new melting peak arises in the heating scans around the melting point of bulk MMM (56 °C). The integral intensity of this peak rises with decreasing charge ratio. The corresponding melting event can be attributed to the melting of (macroscopic) cLNP-DNA complexes consisting of many platelets. The calculated enthalpies of fusion ΔH_{fus} for all melting events and $\Delta H^{\dagger}_{\mathrm{fus}}$ for the peak at 56 °C (integrated in the range 52 - 56 °C, dashed box in the heating run of Fig. S3(a)) are listed in Table SII(b). For the highest DNA loading ($\xi = 0.3$) only large agglomerates are present and no melting peaks of small complexes and remaining individual platelets (temperatures below the dashed boxes) can be observed anymore.

A similar conclusion can be drawn from the cooling curves. Upon addition of DNA the main crystallization peak around 14.6 °C of the super-cooled single emulsion droplets is preceded for charge ratios >0.3 by additional exothermal peaks above 30 °C. The fraction of the enthalpies $\Delta H^{\dagger}_{\mathrm{cry}}$ of these crystallization events (integrated between 30 and 56 °C, dashed box in the cooling runs of Fig. S3(a)) with respect to the total enthalpy of crystallization ΔH_{cry} (integration over all crystallization events in the cooling runs) rise with decreasing charge ratio (Table SII(b)). The ratios $\Delta H^{\dagger}_{\mathrm{fus}}/\Delta H_{\mathrm{fus}}$ and $\Delta H^{\dagger}_{\mathrm{cry}}/\Delta H_{\mathrm{cry}}$ are in good

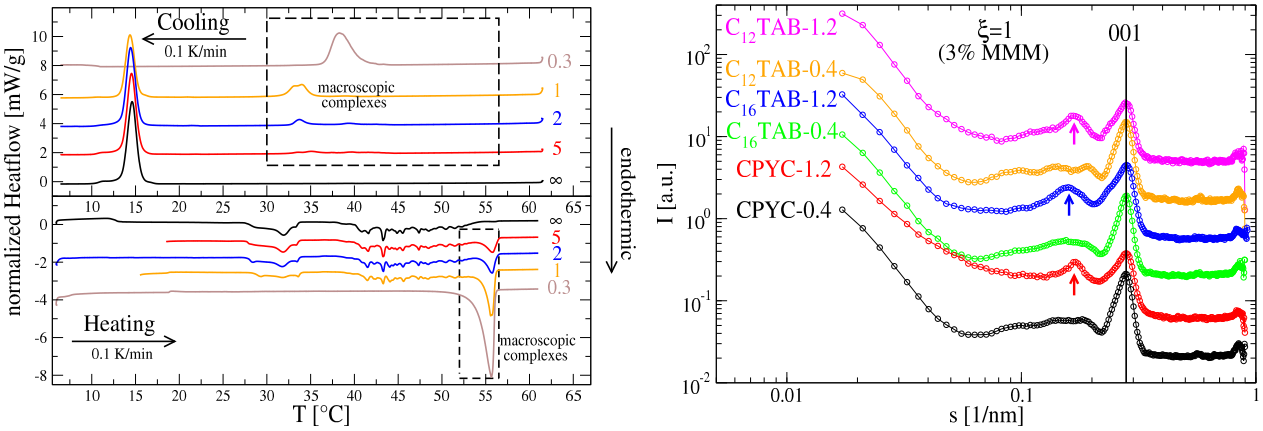

(a) CPYC-1.2 + DNA (3% MMM) (b)

Figure S3: (a) µDSC heating and cooling runs for cLNP-DNA complexes (3% MMM) with CPYC-1.2 at charge ratios ξ between 0.3 and ∞. (b) SAXS patterns taken with the Hecus camera of complexes (3% MMM, fixed charge ratio $\xi = 1$) prepared from different MMM suspensions. For a better representation the curves in (a) are shifted vertically in steps of 2 mW/g (cooling) and −0.9 mW/g (heating), starting from the curve with charge ratio ∞. In (b) the SAXS pattern are shifted by factors of 3, starting from the pattern of CPYC-0.4 at the bottom.

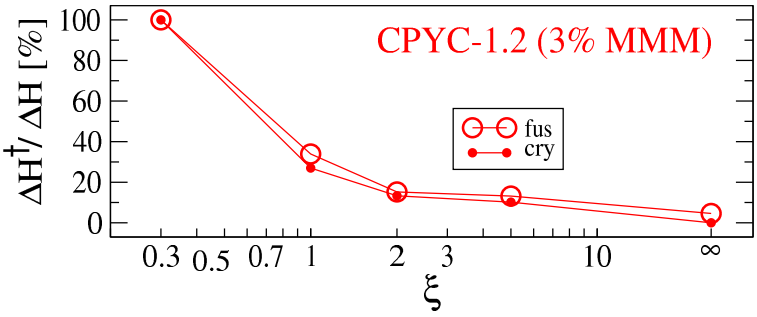

Figure S4: Fraction of macroscopic cLNP-DNA complexes with respect to the total dispersed phase as determined by µDSC ($\Delta H^{\dagger}_{\rm fus}/\Delta H_{\rm fus}$ in heating and $\Delta H^{\dagger}_{\rm cry}/\Delta H_{\rm cry}$ in cooling runs, Table SII(b)) for complexes prepared from CPYC-1.2 for different charge ratios ξ.

agreement (Fig. S4). Thus, these crystallization peaks correspond to the crystallization of larger molten cLNP-DNA agglomerates. For the charge ratio 0.3 any crystallization of molten single platelets or small complexes is missing and the large molten agglomerates recrystallize already between 43.5 °C and 35 °C.

B.2.3 TEM micrograph

Agglomerates of several platelets were found in freeze-fracture TEM micrographs of cLNP-DNA complexes prepared from CPYC-0.4 with the charge ratio 3 (*cf.* Fig. S5). The micrograph suggests a stack-like agglomeration of the platelets. However, as it is demonstrated below, the SAXS patterns of these DNA-complexes can clearly rule out this possibility. The MMM platelets possess an elongated shape with lengths of the long axis ranging typically between 200 and 500 nm.

B.2.4 SAXS measurements

The SAXS patterns for cLNP-DNA complexes (3% MMM), prepared from the native suspensions CPYC-x, C_{16}TAB-x and C_{12}TAB-x with a charge ratio $\xi = 1$, are shown in Fig. S3(b). They do not clearly feature distinct peaks of a lamellar order. Nevertheless, in the s-range between the diffuse small-angle scattering ($s < 0.06\,\mathrm{nm}^{-1}$) and the 001 Bragg peak ($s > 0.22\,\mathrm{nm}^{-1}$), for the complexes prepared from native suspensions with 0.4% of the cationic stabilizer, a broad bump with additional small peaks on top

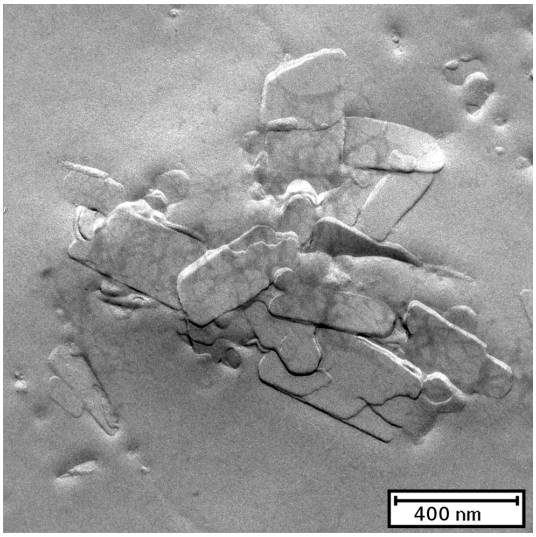

Figure S5: Freeze-fracture TEM micrograph taken from cLNP-DNA complexes (1% MMM) prepared from CPYC-0.4 with a charge ratio $\xi = 3$.

is observed. For complexes prepared from the native suspensions with 1.2% cationic stabilizer a more distinct peak (marked by an arrow) appears at $s = 0.17\,\mathrm{nm}^{-1}$ (CPYC-1.2, C_{12}TAB-1.2) and $s = 0.16\,\mathrm{nm}^{-1}$ (C_{16}TAB-1.2), respectively.
As there is no clear indication of a lamellar order in the SAXS patterns, it can be concluded that the tested suspensions cannot form complexes with a sandwich-like structure of the platelets and DNA.
It is demonstrated below in section C.3, that the SAXS patterns in Fig. S3(b) resemble in the considered s-range those of DNA-complexes prepared with triglyceride-free dispersions, containing only the cationic and nonionic stabilizers. This indicates that the DNA induces a dissociation of the cationic and lecithin molecules from the surface of the platelets and forms complexes with these lipids, while the platelets, being (partially) deprived of their stabilizer molecules, agglomerate in a non-stacked way.
The comparison between the TEM and the SAXS data suggests that freeze-fracture TEM micrographs of such DNA-complexes should be regarded with care. Agglomerates of such platelets could be misleadingly interpreted as complexes with a stacked structure of the platelets. SAXS allows a more reliable differentiation between agglomerates with and without a stacked arrangement of the platelets. This is because, platelet stacks would cause pronounced lamellarly ordered interference peaks in the SAXS patterns, as it is demonstrated for the DNA-complexes with the tripalmitin suspensions in the main article. Furthermore, in contrast to cryo-TEM and freeze-fracture TEM, no particular sample preparation is required for SAXS, and the suspensions can be measured in their native state at ambient temperatures.

C Tripalmitin suspensions

Table SIII: Positions s_b of the bump B and the position (s_{001}) and width (σ_{001}) of the 001 Bragg peak in the SAXS patterns of the native PPP suspensions prepared with S100 or DMPC (Figs. 5(a) and S9(a)). For the DMPC-stabilized suspensions of the PLX-x series two positions are listed for s_b for the bumps B_1 and B_2. Furthermore, the repeat distances d_{st} of PPP platelets in the stacks of the corresponding cLNP-DNA complexes are listed. The mean repeat distance of 14.7 nm for complexes of the DMPC-stabilized PLX-1.2 and PLX-2.0 suspension were found only for some charge ratios and were detected indirectly by an enhancement of the bump B_2 in the SAXS patterns of Figs. S9(c) and S9(d).

	S100				DMPC			
sample	s_b [1/nm]	s_{001} [1/nm]	σ_{001} [1/nm]	d_{st} [nm]	s_b [1/nm]	s_{001} [1/nm]	σ_{001} [1/nm]	d_{st} [nm]
PLX-0.4	0.111	0.236	0.0298	15.4	0.083	0.237	0.0275	11.9
					0.129			
PLX-1.2	-	0.230	0.0328	15.2	0.082	0.230	0.0327	11.6
					0.131			(14.7)
PLX-2.0	-	0.229	0.0344	15.1	0.082	0.231	0.0315	11.4
					0.135			(14.7)
TW-0.4	0.128	0.233	0.0338	15.3	0.092	0.225	0.0372	11.9
TW-0.8	0.128	0.229	0.0359	15.3	0.089	0.223	0.0379	11.7
TW-1.6	0.085	0.215	0.0434	11.2	0.087	0.222	0.0386	11.3
TW-2.5	0.085	0.215	0.0429	11.1	0.087	0.217	0.0413	11.1

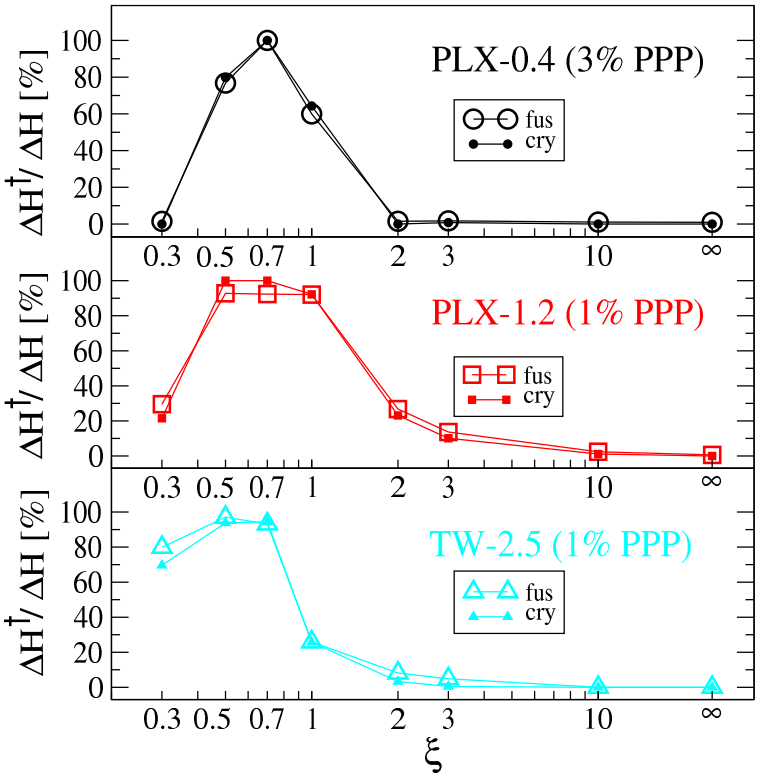

Figure S6: Fractions of macroscopic cLNP-DNA complexes with respect to the total dispersed phase as determined by µDSC for complexes prepared with different charge ratios ξ from PLX-0.4, PLX-1.2 and TW-2.5. The data was taken from Table SIV.

Table SIV: z-averages (d_{PCS}), polydispersity indices (PdI) and enthalpies of fusion (ΔH_{fus}) and crystallization (ΔH_{cry}) for cLNP-DNA complexes prepared from the native suspension (a) PLX-0.4 (3% PPP), (b) PLX-1.2 (1% PPP) and (c) TW-2.5 (1% PPP). Starred fields indicate PCS measurements with $d_{\mathrm{PCS}} > 1\,\mu\mathrm{m}$. ΔH_{fus} and ΔH_{cry} are obtained from the μDSC heating and cooling curves in Fig. 9. $\Delta H^{\dagger}_{\mathrm{fus}}$ denotes the enthalpy of fusion associated with the melting of large platelet agglomerates observed at high temperatures.

(a) PLX-0.4

PCS			μDSC					
ξ	d_{PCS}	PdI	ΔH_{fus}	$\Delta H^{\dagger}_{\mathrm{fus}}$	$\frac{\Delta H^{\dagger}_{\mathrm{fus}}}{\Delta H_{\mathrm{fus}}}$	ΔH_{cry}	$\Delta H^{\dagger}_{\mathrm{cry}}$	$\frac{\Delta H^{\dagger}_{\mathrm{cry}}}{\Delta H_{\mathrm{cry}}}$
[-]	[nm]	[-]	[J/g]	[J/g]	[%]	[J/g]	[J/g]	[%]
0.3	*	*	5.60	0.08	1.4	-5.76	-0.00	0.0
0.5	*	*	6.54	5.02	76.8	-5.85	-4.67	79.8
0.7	721.3	0.37	6.88	6.88	100.0	-6.14	-6.14	100.0
1	718.3	0.31	6.52	3.91	60.0	-5.91	-3.80	64.3
2	292.2	0.25	6.04	0.09	1.5	-5.89	-0.00	0.0
3	185.7	0.26	5.27	0.09	1.7	-4.99	-0.04	0.8
10	146.5	0.26	5.61	0.06	1.1	-5.32	-0.00	0.0
∞	136.6	0.25	5.48	0.05	0.9	-5.26	-0.00	0.0

(b) PLX-1.2

PCS			μDSC					
ξ	d_{PCS}	PdI	ΔH_{fus}	$\Delta H^{\dagger}_{\mathrm{fus}}$	$\frac{\Delta H^{\dagger}_{\mathrm{fus}}}{\Delta H_{\mathrm{fus}}}$	ΔH_{cry}	$\Delta H^{\dagger}_{\mathrm{cry}}$	$\frac{\Delta H^{\dagger}_{\mathrm{cry}}}{\Delta H_{\mathrm{cry}}}$
[-]	[nm]	[-]	[J/g]	[J/g]	[%]	[J/g]	[J/g]	[%]
0.3	*	*	1.93	0.57	29.5	-1.91	-0.41	21.5
0.5	*	*	2.08	1.93	92.8	-1.72	-1.72	100.0
0.7	*	*	2.09	1.93	92.3	-1.75	-1.75	100.0
1	*	*	2.02	1.86	92.1	-1.80	-1.66	92.2
2	730.5	0.27	1.83	0.49	26.8	-1.82	-0.42	23.1
3	239.6	0.33	1.83	0.25	13.7	-1.84	-0.20	10.9
10	128.6	0.26	1.66	0.04	2.4	-1.75	-0.02	1.1
∞	123.7	0.25	1.61	0.01	0.6	-1.79	-0.00	0.0

(c) PLX-2.5

PCS			μDSC					
ξ	d_{PCS}	PdI	ΔH_{fus}	$\Delta H^{\dagger}_{\mathrm{fus}}$	$\frac{\Delta H^{\dagger}_{\mathrm{fus}}}{\Delta H_{\mathrm{fus}}}$	ΔH_{cry}	$\Delta H^{\dagger}_{\mathrm{cry}}$	$\frac{\Delta H^{\dagger}_{\mathrm{cry}}}{\Delta H_{\mathrm{cry}}}$
[-]	[nm]	[-]	[J/g]	[J/g]	[%]	[J/g]	[J/g]	[%]
0.3	*	*	1.94	1.55	79.9	-1.94	-1.35	69.6
0.5	*	*	2.01	1.95	97.0	-1.95	-1.83	93.8
0.7	*	*	2.06	1.92	93.2	-1.96	-1.85	94.4
1	*	*	1.97	0.51	25.9	-1.91	-0.49	25.7
2	*	*	1.84	0.15	8.2	-1.83	-0.06	3.3
3	702.5	0.30	1.84	0.09	4.9	-1.82	-0.01	0.5
10	212.4	0.29	1.65	0.00	0.0	-1.83	-0.00	0.0
∞	61.6	0.38	1.76	0.00	0.0	-1.83	-0.00	0.0

C.1 Replacing S100 by DMPC

Table SV: PCS measured z-averages of the hydrodynamic diameter (d_{PCS}), polydispersity indices (PdI) and enthalpy of fusion (ΔH_{fus}) and crystallization (ΔH_{cry}) (obtained from the μDSC heating and cooling runs in Fig. S8) for the native PPP suspensions stabilized with DMPC, PLX or TW, and different amounts of DODAB. $\Delta H^*_{\mathrm{fus}}$ denotes the enthalpy of fusion associated with the melting of particles with the unknown PPP modification.

	PCS		μDSC			
sample	d_{PCS} [nm]	PdI [-]	ΔH_{fus} [J/g]	$\Delta H^*_{\mathrm{fus}}$ [J/g]	$\frac{\Delta H^*_{\mathrm{fus}}}{\Delta H_{\mathrm{fus}}}$ [%]	ΔH_{cry} [J/g]
PLX-0.4	187.9	0.24	18.7	7.3	39.0	-16.9
PLX-1.2	180.9	0.21	19.4	8.5	43.8	-17.3
PLX-2.0	126.1	0.26	19.4	10.7	55.2	-18.2
TW-0.4	112.1	0.27	18.7	10.8	58.7	-17.0
TW-0.8	101.4	0.30	19.3	11.8	61.1	-18.3
TW-1.6	102.0	0.26	n/a	n/a	n/a	n/a
TW-2.5	87.2	0.31	19.4	14.1	72.7	-18.9

The influence of the lecithin stabilizer on the morphology of the cLNP and the internal structure of the nanocomposites was investigated. For this purpose, the lecithin blend S100 in the native suspensions was substituted by an equivalent amount of the fully saturated lecithin DMPC. The obtained suspensions are stable and provided for the TW-x series very similar particle size distributions as for the S100-stabilized suspensions (Table SV). The size distributions for the PLX-x series are again less broad and indicate larger particles, compared to the dispersions of the TW-x series.

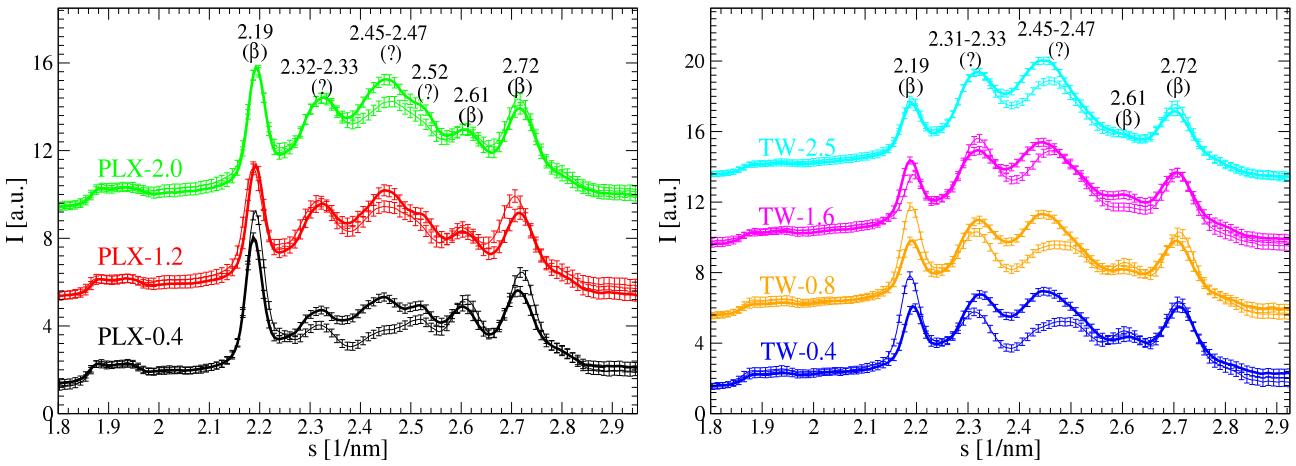

(a) Native PPP PLX-x suspensions with DMPC or S100

(b) Native PPP TW-x suspensions with DMPC or S100

Figure S7: WAXS patterns measured at the ID02 beamline for the native PPP suspensions stabilized with DMPC (thick lines) or S100 (thin lines), different amounts of DODAB and (a) PLX or (b) TW. The positions for the strongest reflections of β-PPP at 2.19, 2.61 and 2.72 nm^{-1} are marked. Additionally, the peaks of the unknown modification at 2.32 and 2.46 nm^{-1} are marked. For a better representation the diffractograms were shifted vertically and every second data point was omitted.

The WAXS patterns of the native DMPC-stabilized suspensions are visualized in Fig. S7. The WAXS patterns of the corresponding S100-stabilized suspensions from Fig. 3 are included for a direct comparison. Obviously, the scattering contributions, linked to the unknown PPP modification, are enhanced for the DMPC-stabilized suspensions with respect to their S100-stabilized counterparts, particularly for the PLX-x series, TW-0.4 and TW-0.8 .

The µDSC scans for the native suspensions are visualized in Fig. S8. The heating curves can be again divided into two sections. The first section from 30 °C up to 50 °C (PLX-x) and 48 °C (TW-x), respectively,

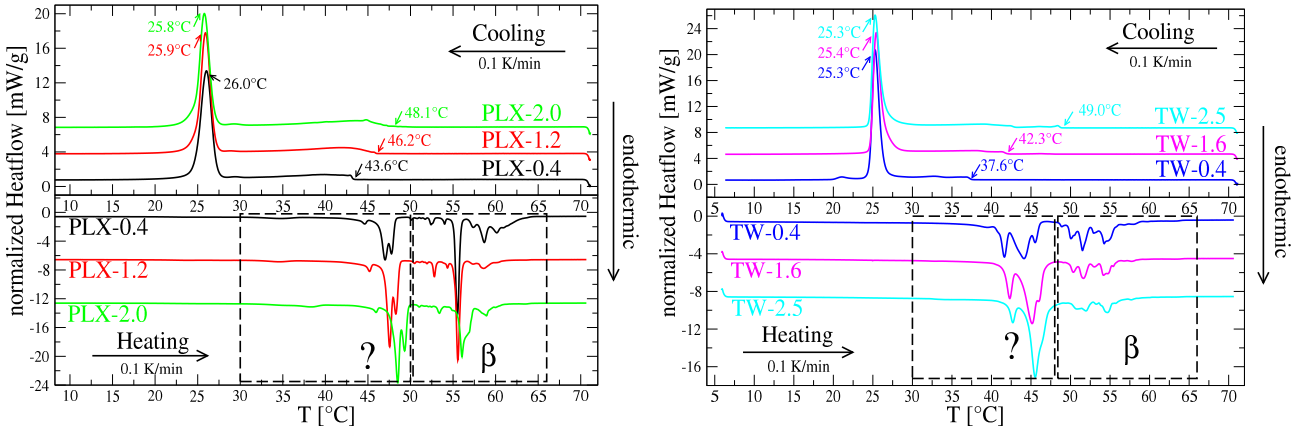

(a) Native PPP PLX-x suspensions with DMPC

(b) Native PPP TW-x suspensions with DMPC

Figure S8: µDSC heating and cooling runs for the native PPP suspensions stabilized with DMPC, varying amounts of DODAB, and (a) PLX or (b) TW. The heating and cooling curves were shifted vertically in steps of 6 and $-3\,\mathrm{mW/g}$, respectively, with respect to the curves for PLX-0.4 and TW-0.4. The dashed boxes in the heating curves mark the temperature ranges associated with the melting of platelets in the unknown (?) and β-PPP modification, respectively.

can be linked to the unknown PPP modification, the second section up to 66 °C to the β-modification. As for the S100-stabilized suspensions, the amount of the enthalpy of fusion in the first section $\Delta H^*_{\mathrm{fus}}$ (integrated in the dashed box marked with the question mark, 30 to 50 °C (PLX-x) or 48 °C (TW-x)) grows with rising DODAB concentration at the expense of the second section, and the melting peak shifts slightly to higher temperatures. The relative amount of the unknown PPP modification $\Delta H^*_{\mathrm{fus}}/\Delta H_{\mathrm{fus}}$ is listed for all native PPP suspensions in Table SV and visualized in Fig. 10 in the article. For the DMPC-stabilized dispersions, $\Delta H^*_{\mathrm{fus}}/\Delta H_{\mathrm{fus}}$ is even for low concentrations of DODAB (TW-0.4 and PLX-0.4) much higher than for those with S100. For higher DODAB concentrations, the fraction increases to more than 70% for TW-2.5. Thus, from the WAXS and micro-calorimetric data, it is apparent that not only DODAB, but also DMPC with its two saturated acyl chains promotes the formation of the unknown PPP modification.

The main crystallization peaks for the TW-x and PLX-x samples are in the range between 25 °C and 26 °C (*cf.* Fig. S8) and, thus, at very similar temperatures as for the suspensions prepared with S100 and high amounts of DODAB (PLX-1.2, PLX-2.0, TW-1.6 and TW-2.5 in Fig. 4 in the main article). All cooling curves in Fig. S8, even those with very low amounts of DODAB (PLX-0.4, TW-0.4), exhibit one or more pre-crystallization events (those with the highest temperature are marked by arrows). Their highest onset temperatures rise with the amount of DODAB from 43.6 °C (PLX-0.4) to 48.1 °C (PLX-2.0) and from 37.6 °C (TW-0.4) to 49.0 °C (TW-2.5), respectively. The temperatures of these pre-crystallization events are generally higher than in the case of S100. Similarly to the S100-stabilized suspensions these pre-transitions can be most probably attributed to a pre-crystallization of the saturated acyl chains of the DODAB and here additionally, DMPC molecules at the surface of the emulsion droplets. For DMPC-stabilized PPP suspensions similar pre-transitions were found starting at 40 °C [8], in good agreement with the temperatures of 43.6 °C (PLX-0.4) and 37.6 °C (TW-0.4), found here for DMPC-stabilized suspensions with small concentrations in DODAB.

The SAXS patterns of the native DMPC-stabilized suspensions are visualized in Fig. S9(a). Particularly, in the range between the 001 Bragg peak and the diffuse small-angle scattering, the SAXS patterns of the PLX-x series, TW-0.4 and TW-0.8 differ from those of their S100-stabilized counterparts (*cf.* Fig. 5a in the article). A bump at $s_{\mathrm{b}} = 0.084\,\mathrm{nm}^{-1}$ for the PLX-x series (marked with B_1 in Fig. S9(a)), and, more pronounced for the TW-x series at $0.090\,\mathrm{nm}^{-1}$ (marked with B), is found (positions s_{b} listed in Table SIII). For TW-1.6 and TW-2.5 the scattering patterns and the positions of B are very similar to those of the corresponding S100-stabilized suspensions. For the suspensions of the PLX-x series an additional small peak (marked with B_2 in Fig. S9(a)) can be observed in the s-range between 0.13 and $0.135\,\mathrm{nm}^{-1}$, and thus, at a similar position as the bump in the S100-stabilized suspension of the PLX-series, TW-0.4 and

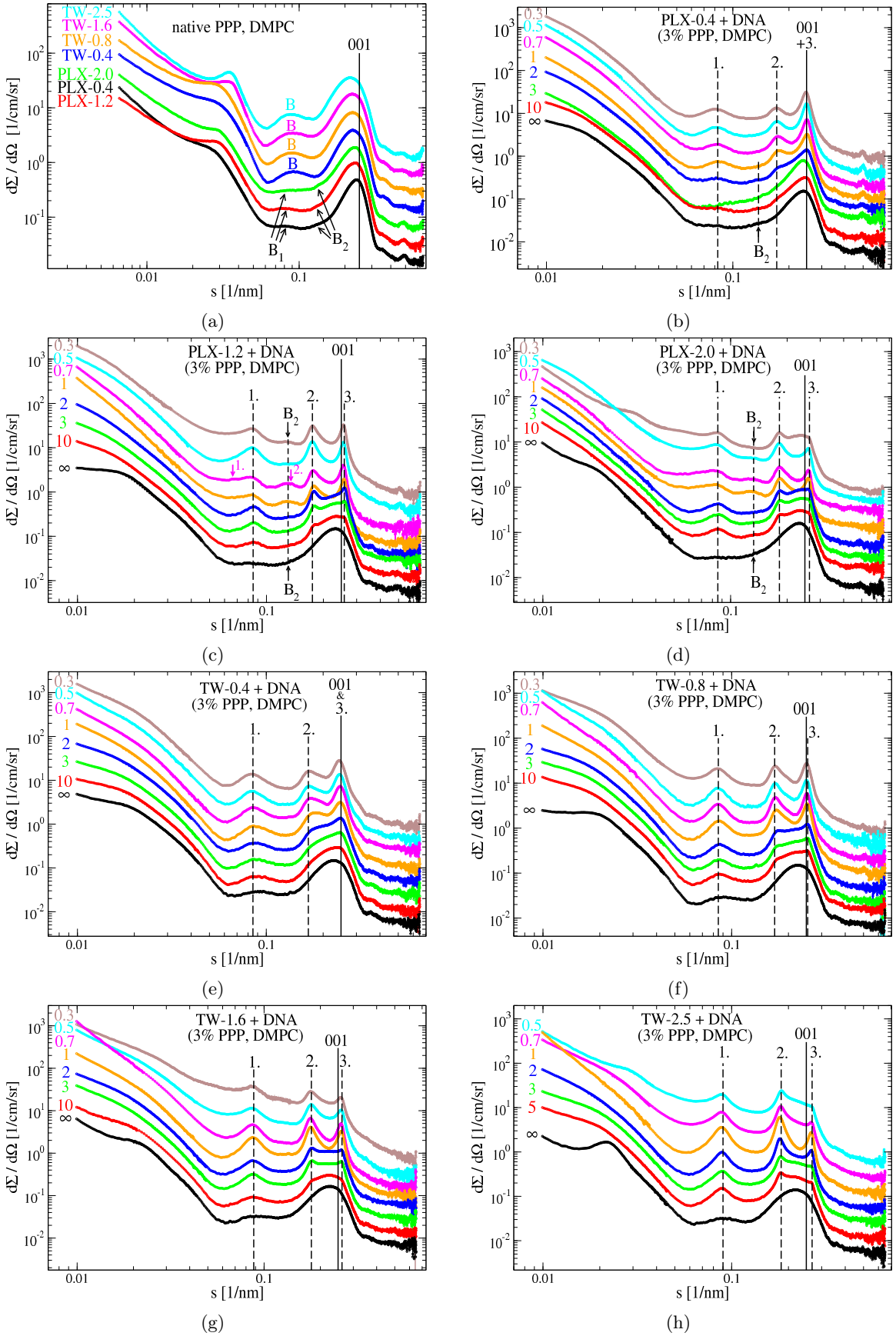

Figure S9: SAXS patterns (ID02 beamline) for (a) the native PPP suspensions stabilized with DMPC, PLX or TW and different amounts of DODAB and (b-h) cLNP-DNA complexes (3% PPP) with charge ratios in the range ∞ to 0.3 prepared from: (b) PLX-0.4, (c) PLX-1.2, (d) PLX-2.0 (e) TW-0.4, (f) TW-0.8, (g) TW-1.6 and (h) TW-2.5. For clarity, the SAXS patterns were scaled by multiples of 2, starting from the solid black curve at the bottom. The position of the 001 Bragg reflection for bulk β-PPP and the three orders of the stack-related interferences are marked by vertical lines.

TW-0.8.
Again the 001 Bragg peak broadens and shifts to lower s-values with rising DODAB concentration. The positions s_{001} and widths σ_{001} of the 001 Bragg peaks (Table SIII) are nearly the same as in the case of the S100-stabilized versions of PLX-x, TW-1.6 and TW-2.5. For TW-0.4 and TW-0.8 which exhibited the largest increase in the unknown PPP modification with its small platelets, the 001 Bragg peak is shifted to lower s and became broader than for the corresponding suspensions with S100.
The differences in the SAXS patterns of the native DMPC-stabilized suspensions of the PLX-x series, TW-0.4 and TW-0.8 with respect to their S100-stabilized counterparts already indicate different structures for their cLNP-DNA complexes. Indeed, all SAXS patterns of the cLNP-DNA complexes (3% PPP), prepared from the DMPC-stabilized suspensions, exhibit stack-related interferences, associated with repeat distances between of 11.1 and 11.9 nm, respectively (*cf.* Fig. S9 and Table SIII). Again, the repeat distances decrease slightly with increasing amount of DODAB (from 11.9 nm (PLX-0.4, TW-0.4) to 11.4 nm (PLX-2.0) and 11.1 nm (TW-2.5)).
Interestingly, in the SAXS patterns of the complexes prepared from the native PLX-x suspensions (Figs. S9(b), S9(c) and S9(d)), the second bump B_2 is still present (in particular for PLX-1.2 and PLX-2.0 and at charge ratios close to the isoelectric point, 0.7 and 1). But, in contrast to the SAXS patterns of their S100-stabilized counterparts, almost no lamellar order, corresponding to a repeat distance of about 15 nm can be found. Thus, it the thicker β-PPP platelets, which are most probably linked to the bump B_2 and caused repeat distances of about 15 nm in the case of the complexes of S100-stabilized PLX-x suspensions, are less frequently integrated into stacks as the smaller and thinner ones of the unknown PPP modification, which are most probably linked to the bump B_1 and form the stacks with repeat distances between 11 and 12 nm. For complexes from PLX-1.2 and PLX-2.0 with charge ratios around the isoelectric point, a small amount of the thicker platelets forms additional stacks with repeat distances of about 15 nm, since B_2 is enhanced by an interference between the scattering from B_2 and the stack-related scattering. For the complex prepared from PLX-1.2 with the charge ratio 0.7 even a small first order reflection at $s = 0.068\,\mathrm{nm}^{-1}$ (corresponding to $d_{\mathrm{st}} = 14.7\,\mathrm{nm}$) of this stack-related scattering can be found (marked by arrows in Fig. S9(c); the second order coincides with the position of B_2).
The positions s_{b} of the observed bumps B (B_1 and B_2) in the scattering patterns of the native S100- and DMPC-stabilized suspensions (Figs. 5(a) and S9(a)), which are most probably linked to the form factor or an unknown internal structure of the platelets, are clearly correlated to the amount of the unknown PPP modification and the repeat distance of the platelets in the cLNP-DNA complexes. As shown in Fig. S10 and Fig. 10 in the main article, a repeat distance of about 15 nm is always linked to a bump position between 0.11 and 0.13 nm^{-1} in the SAXS patterns and a fraction $\lesssim 40\%$ of the unknown PPP modification for the dispersed PPP. By contrast, native suspensions with $\gtrsim 55\%$ of the unknown PPP modification feature bumps located between 0.083 and 0.092 nm^{-1} and produce always cLNP-DNA complexes with repeat distances between about 11 nm and 12 nm. For the transitional range between 40 and 55%, the native suspensions feature both bumps but their nanocomposites consist predominantly of the thinner platelets of the unknown PPP modification, since the intensity of the stack-related maxima, associated with repeat distances between 11 and 12 nm, prevails the peak intensities of stacks with repeat distances of about 15 nm (if they exist at all).

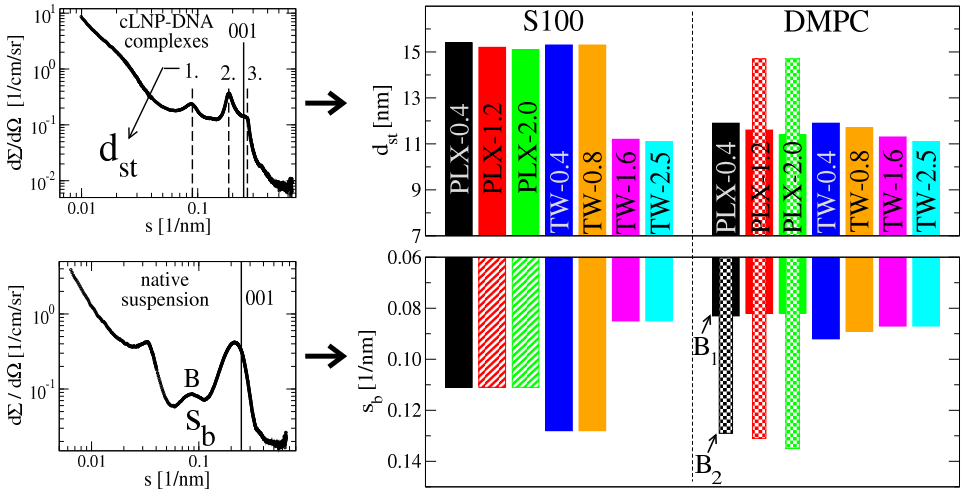

Figure S10: Correlation between the mean repeat distances d_{st} of the nanocrystals in cLNP-DNA complexes (upper part, data from Table SIII) and the position of the bump s_{b} in the SAXS patterns of their corresponding native suspension (lower part, Figs. 5(a) and S9(a) and Table SIII). Native PPP suspensions stabilized by S100 (left) or DMPC (right), PLX or TW, and different DODAB concentrations were studied. For the S100-stabilized PLX-1.2 and PLX-2.0 suspensions, where no bump was directly visible in the SAXS patterns, and its existence manifested only in the SAXS patterns of their cLNP-DNA complexes, the same value for s_{b} was used as for the S100-stabilized PLX-0.4 suspension (diagonally striped bars). For the DMPC-stabilized suspensions of the PLX-x series two bump positions were observed (filled bars for B_1 and chequered bars for B_2). The repeat distance of 14.7 nm (chequered bars in the upper part), present only marginally for some charge ratios of the complexes of the DMPC-stabilized PLX-1.2 and PLX-2.0 suspensions, were detected indirectly by an enhancement of the bump B_2 in the SAXS patterns of Figs. S9(c) and S9(d).

C.2 XNPPSA Fits

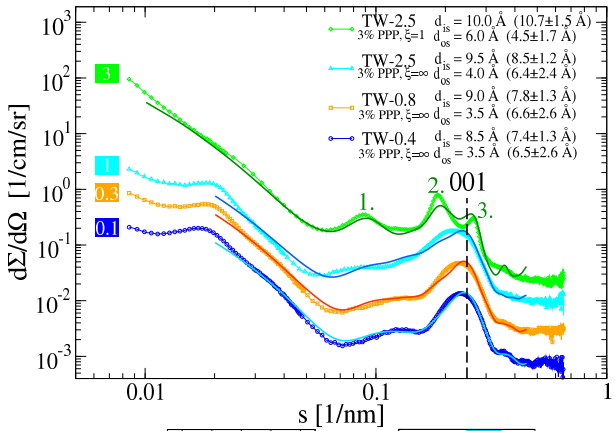

(a) TW-0.4, 3% PPP, $\xi = \infty$

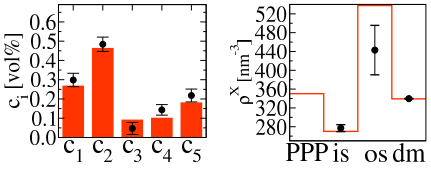

(b) TW-0.8, 3% PPP, $\xi = \infty$

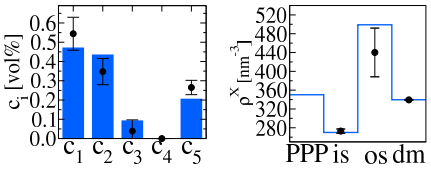

(c) TW-2.5, 3% PPP, $\xi = \infty$

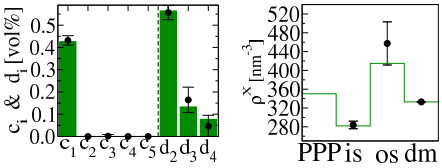

(d) TW-2.5, 3% PPP, $\xi = 1$

Figure S11: SAXS patterns of dilute suspensions of TW-0.4, TW-0.8 and TW-2.5 (3% PPP, $\xi = \infty$) and cLNP-DNA complexes with TW-2.5 (3% PPP, $\xi = 1$). The XNPPSA fits are drawn as solid lines. For complexes the simulated stacks consist of platelets with a thickness of two unit cells PPP. The fitted distributions of the platelet thicknesses (c_i) and stack sizes (d_i), electron densities (ρ^X) of the inner and outer shell (is,os) and the dispersion medium (dm) are plotted, too. For a better representation the patterns were multiplied by factors indicated on the left side of each curve.

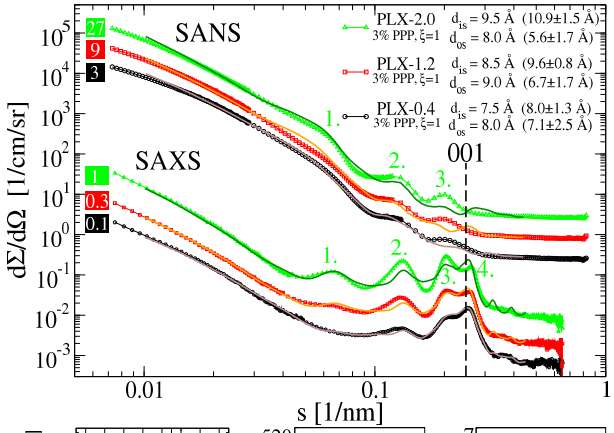

(a) PLX-0.4, 3% PPP, $\xi = 1$

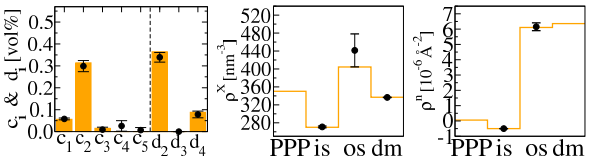

(b) PLX-1.2, 3% PPP, $\xi = 1$

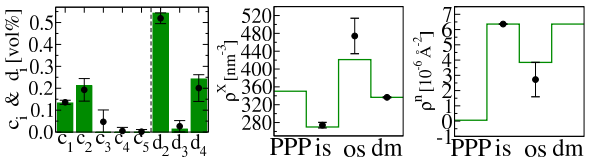

(c) PLX-2.0, 3% PPP, $\xi = 1$

Figure S12: SAXS and SANS patterns of cLNP-DNA complexes of the PLX-x series (3% PPP, $\xi = 1$). The XNPPSA fits are drawn as solid lines. The simulated stacks consisted of platelets with a **thickness of three unit cells PPP**. The fitted platelet thickness and stack size distributions (coefficients c_i and d_i) are visualized, too.

C.3 Suspensions without PPP

Dispersions equivalent to PLX-0.4 and TW-2.5, but without PPP, were prepared by high-pressure homogenization and, along with their DNA-complexes, studied by SAXS. In Fig. S13(a), the SAXS patterns for the native suspension PLX-0.4 and its cLNP-DNA complexes, as well as the patterns for their PPP-free counterparts are visualized. The native, PPP-free PLX-0.4 suspension exhibits four broad peaks at 0.083, 0.14, 0.195, and 0.256 nm^{-1} (marked by arrows) on top of a broad bump, stretching from about 0.055 to 0.30 nm^{-1}. From the SAXS patterns alone, it is difficult to draw definite conclusions on the structures causing these peaks. The broad underlying bump is most probably related to the characteristic form factors of lecithin and DODAB bilayers, which are typically found in a similar s-range [13]. The four peaks do not fit very well to a lamellar order.

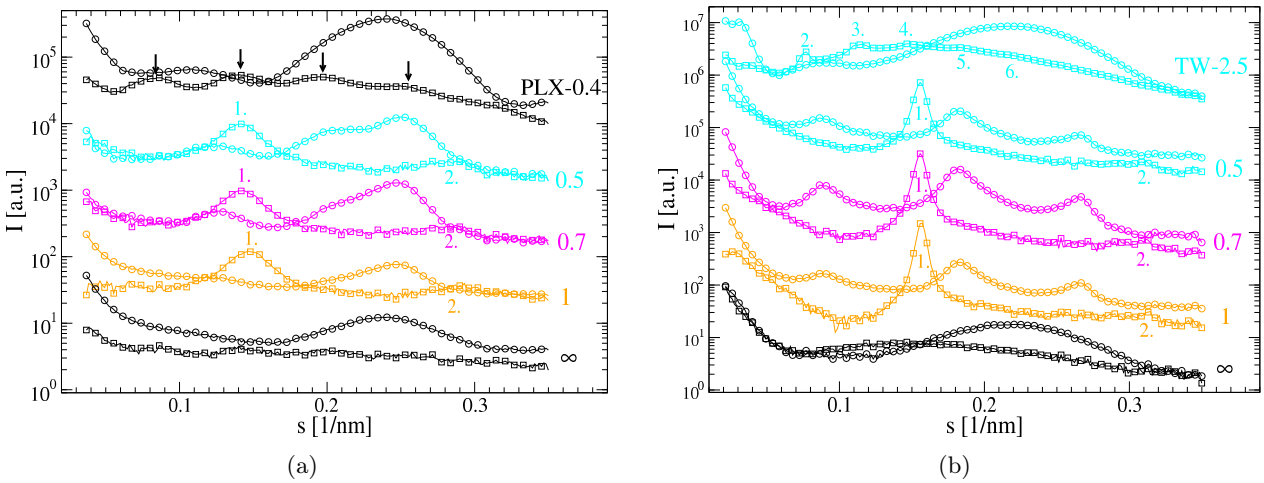

Figure S13: SAXS patterns (A2 beamline) of cLNP-DNA complexes prepared from PPP-containing and PPP-free dispersions: (a) PLX-0.4 and (b) TW-2.5. Curves with (○) and without (□) PPP are shown. The two curves on the top correspond to the native suspensions without DNA. For the complexes, the native dispersions were diluted by a factor of 10, the charge ratios range from 0.5 to ∞. For clarity the curves were shifted vertically.

In Fig. S13(b) the SAXS patterns for the PPP-containing and PPP-free native suspension TW-2.5 and their cLNP-DNA complexes are displayed. For the native, PPP-free TW-2.5 suspension five peaks at 0.038, 0.0766, 0.114, 0.148, 0.183, and 0.220 nm^{-1} on top of a broad bump can be identified. The bump itself could be again related to the form factor of lecithin and DODAB bilayers or cylindrical TW micelles [14]. The peaks fit very well to the second to sixth orders of a structure with a lamellar order of 26.6 nm. The situation for the triglyceride-free cLNP-DNA complexes is completely different with respect to their PPP-containing counterparts. In contrast to the repeat distances of about 15 nm (PLX-0.4) and 11 nm (TW-2.5) for the PPP-containing cLNP-DNA complexes, the SAXS patterns for the PPP-free complexes exhibit two characteristic peaks, which correspond to a lamellar order of about 6.7 nm (PLX-0.4) and 6.4 nm (TW-2.5). These structures can be attributed to multilamellar structures of S100 or mixed S100-DODAB bilayers. An intercalation of the DNA in the water layers between the bilayers is very likely. Similar sandwich-like structures were reported for DNA-complexes with the lecithin DOPC (1,2-dioleoyl-sn-glycero-3-phosphocholine) in the presence of divalent cations (repeat distances between 7.4 and 8.3 nm [15]) and with mixtures of DOPC with DOTAP (6.5 ± 0.2 nm [16]).
Based on these data and in accordance with the previous findings, the strong interference maxima in the scattering patterns of the cLNP-DNA complexes with the PPP-containing suspensions cannot stem from structures built from DNA and the stabilizers alone.
Interestingly, the SAXS patterns for the PPP-free suspensions and their cLNP-DNA complexes bear a certain resemblance to the scattering patterns of the complexes from the MMM suspensions in section B of the Supplementary Material. The SAXS patterns for the cLNP-DNA complexes from CPYC-0.4 and CPYC-1.2 at a charge ratio $\xi = 1$ are contrasted in Fig. S14 with the SAXS patterns of the native PPP-free PLX-0.4 suspension and the DNA-complexes ($\xi = 1$) of the PPP-free PLX-0.4 and TW-2.5 suspensions,

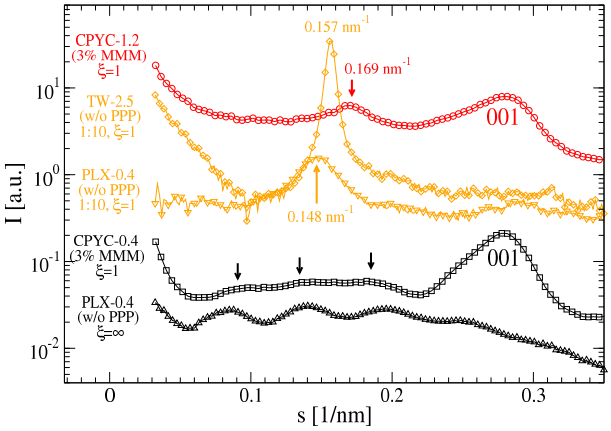

(a)

Figure S14: SAXS patterns (Hecus camera) for cLNP-DNA complexes (3% MMM, $\xi = 1$) prepared from the MMM suspensions CPYC-0.4 (□) and CPYC-1.2 (○). The SAXS patterns (A2 beamline) for the PPP-free, native suspension PLX-0.4 (△) and cLNP-DNA complexes prepared from the PPP-free suspensions PLX-0.4 and TW-2.5 (10-fold dilution from the native suspensions) at a charge ratio $\xi = 1$ (▽ and ◇, respectively) are shown, too. For clarity the curves were shifted vertically.

respectively (the SAXS patterns for the cLNP-DNA complexes prepared from CPYC-0.4 and CPYC-1.2 are representative for the patterns of the cLNP-DNA complexes with C_{16}TAB and C_{12}TAB (Fig. S3(b))). For the cLNP-DNA complexes from CPYC-0.4, the broad bump with its small peaks on top (marked by black arrows) in the s-range 0.06 - 0.22 nm^{-1} exhibits a certain similarity to the pattern of the PPP-free PLX-0.4 suspension.

For higher amounts of CPYC and DNA (complexes prepared from CPYC-1.2), the single broad peak (marked by an arrow) might stem from multilamellar structures of S100 or a mixture of S100 and CPYC (repeat distance 5.9 nm), similarly as it was found for the PPP-free DNA-complexes from the PPP-free PLX-0.4 and TW-2.5 suspensions, which exhibit a peak at slightly smaller s-values.

Thus, addition of DNA to the MMM suspensions might lead to a partial detachment of the S100 and single-tailed cationic surfactant (CPYC, C_nTAB) molecules from the MMM platelets. The released stabilizer molecules might form similar lipid or lipid-DNA structures as in the triglyceride-free dispersions while the MMM platelets agglomerate in a non-stacked arrangement due to an adsorption of the DNA or a lack of stabilizer molecules on their surfaces. In the case of the studied PPP suspensions which are stabilized by a blend of S100, the double-tailed, cationic surfactant DODAB and PLX / TW, the PLX and TW molecules which are crucial to inhibit a gelation of the native suspensions upon crystallization might also help to prevent such a release of stabilizer molecules upon interaction with the DNA and, thus, to facilitate the formation of such stacked nanocomposites.

References

[1] M. Schmiele, T. Schindler, T. Unruh, S. Busch, H. Morhenn, M. Westermann, F. Steiniger, A. Radulescu, P. Lindner, R. Schweins and P. Boesecke, *Phys. Rev. E*, 2013, **87**, 062316.

[2] J. F. Nagle and S. Tristram-Nagle, *Biochim. Biophys. Acta, Rev. Biomembr.*, 2000, **1469**, 159–195.

[3] H. Bunjes, *Curr. Opin. Colloid Interface Sci.*, 2011, **16**, 405–411.

[4] K. Westesen and B. Siekmann, *Int. J. Pharm.*, 1997, **151**, 35–45.

[5] T. Unruh, H. Bunjes, K. Westesen and M. H. J. Koch, *J. Phys. Chem. B*, 1999, **103**, 10373–10377.

[6] H. Bunjes, K. Westesen and M. H. Koch, *Int. J. Pharm.*, 1996, **129**, 159–173.

[7] H. Bunjes, M. H. J. Koch and K. Westesen, *Langmuir*, 2000, **16**, 5234–5241.

[8] H. Bunjes and M. H. J. Koch, *J. Controlled Release*, 2005, **107**, 229–243.

[9] F. Zhang, J. Ilavsky, G. Long, J. Quintana, A. Allen and P. Jemian, *Metall. Mater. Trans. A*, 2010, **41**, 1151–1158.

[10] A. van Langevelde, R. Peschar and H. Schenk, *Acta Crystallogr., Sect. B*, 2001, **57**, 372–377.

[11] T. Unruh, K. Westesen, P. Bösecke, P. Lindner and M. H. J. Koch, *Langmuir*, 2002, **18**, 1796–1800.

[12] A. Illing, T. Unruh and M. Koch, *Pharm. Res.*, 2004, **21**, 592–597.

[13] P. Saveyn, P. Van der Meeren, M. Zackrisson, T. Narayanan and U. Olsson, *Soft Matter*, 2009, **5**, 1735–1742.

[14] H. Aizawa, *J. Appl. Cryst.*, 2010, **43**, 630–631.

[15] D. Uhríková, M. Hanulová, S. S. Funari, R. S. Khusainova, F. Šeršeň and P. Balgavý, *Biochim. Biophys. Acta, Biomembr.*, 2005, **1713**, 15–28.

[16] J. O. Rädler, I. Koltover, T. Salditt and C. R. Safinya, *Science*, 1997, **275**, 810–814.